Impact of water vapor on stratospheric temperature after the 2022 Hunga Tonga eruption: direct radiative cooling versus indirect warming by facilitating large particle formation

Xi Chen[1,2,*], Jun Wang[1,2,3,*], Meng Zhou[2,4], Zhendong Lu[2,4], Lyatt Jaegle[5], Luke D. Oman[6], Ghassan Taha[6,7]

[1]Department of Chemical and Biochemical Engineering and Iowa Technology Institute, The University of Iowa; Iowa City, IA 52242, USA.

[2]Center for Global and Regional Environmental Research, The University of Iowa; Iowa City, IA 52242, USA.

[3]Department of Physics and Astronomy, The University of Iowa; Iowa City, IA 52242, USA.

[4]Interdisciplinary Graduate Program in Informatics, The University of Iowa; Iowa City, IA 52242, USA

[5]Department of Atmospheric Sciences, University of Washington; Seattle, WA 98195, USA

[6]Goddard Space Flight Center, National Aeronautics and Space Administration; Greenbelt, MD 20771, USA

[7]GESTAR II, Morgan State University; Baltimore, MD 21251, USA

*Corresponding authors: Xi Chen; Jun Wang

Email: xi-chen-4@uiowa.edu; jun-wang-1@uiowa.edu

Classification: Physical Sciences; Earth, Atmospheric, and Planetary Sciences.

Keywords: Hunga eruption, water vapor, volcanic aerosols, climate impact.

This PDF file includes:

Main Text
Figures 1 to 5

Abstract

The unprecedented water vapor amount (WV, 150-160 Tg) injected by the 2022 eruption of Hunga Tonga–Hunga Ha'apai not only directly cooled the stratosphere, but also facilitated the formation and growth of sulfate particles, indirectly heating it. Here, we developed analytical models constrained by satellite observations to quantify these contrasting roles of WV in stratospheric temperature perturbations. Our analysis revealed that condensation and nucleation processes facilitated by abundant WV accounted for approximately 90% of the observed particle radius growth, from 0.1-0.2 μm to 0.35-0.45 μm. Despite increased aerosol extinction due to particle growth, a cooling of up to -4 K was observed in the mid-stratosphere, persisting for over a year since February, with over 60% attributed to WV radiative cooling. Conversely, in the lower stratosphere, ~50% of the observed 1-2 K warming was attributed to the radiative heating of large particles that formed in upper layers and settled down gravitationally.

Main Text

Introduction

Breaking the record set by the 1991 Mt. Pinatubo eruption, volcanic clouds overshooting tops exceeding 50 km were captured by satellite observations after the powerful explosion of the Hunga Tonga–Hunga Ha'apai (HT) volcano (also referred to as the Hunga eruption in the volcanology community) (175.38W, 20.54S, (5)) at ~4:10 UTC on 15 January 2022 (6-8). As reported by the Global Volcanism Program (GVP) (5), this powerful explosion was assigned a Volcanic Explosivity Index (VEI) of 5 (9). Originating below the ocean, the HT eruption generated tsunami waves that propagated across ocean basins (12-14). Additionally, the explosion triggered rapid atmospheric pressure disturbances that propagated as Lamb waves (10). These disturbances led to remarkable phenomena, including globally detected infrasound (0.01–20 Hz), long-range (~10,000 km) audible sound (11), and ionospheric plasma perturbations, which were observed through global ground-based and satellite measurements (15, 16). Sulfur dioxide (SO_2) emissions from the HT eruption have been assessed in recent studies (8, 9, 17-20) from various satellite measurements, including the Microwave Limb Sounder (MLS), the Ozone Monitoring Instrument (OMI), the Tropospheric Monitoring Instrument (TROPOMI), the Earth Polychromatic Imaging Camera (EPIC), the Ozone Mapping and Profiler Suite (OMPS), and the Infrared Atmospheric Sounding Interferometer (IASI). Although these satellite instruments differ in observation mode (nadir or limb), detection technique (ultraviolet, microwave or infrared), spatial resolution, and coverage, most estimates place SO_2 burden at ~0.4-0.5 Tg with a maximum of > 1.0 Tg observed by IASI a few days after 15 January; this is relatively small compared to past volcanic eruptions (8, 9, 17-20). In addition to the unusual injection height resulting from the tremendous explosive energy, the HT eruption was also distinguished by the richness of its water vapor (WV) injection into the stratosphere (18, 21-24). This resulted from the interaction between the surrounding ocean water and the hot magma in pyroclastic flows, leading to the entrainment of significant amounts of WV into the eruption plumes (18, 25-28). Within a few days, stratospheric SO_2 was oxidized to sulfuric acid (H_2SO_4) vapor by hydroxyl radicals, followed by nucleation, condensation, and coagulation, leading to particle formation and growth, as observed by satellites sensors and ground-based lidars (7, 23, 29).

Tropospheric WV and other greenhouse gases absorb most of the Earth's emitted longwave infrared (LW) radiation, heating the lower atmosphere due to their high abundance. In the stratosphere, where WV concentrations are typically low, any increase in WV within a vertical layer (regardless of its thickness) significantly enhances both absorptivity and emissivity in the LW spectrum within that layer. However, because only a small fraction of terrestrial LW radiation reaches the stratosphere, the increase in LW absorptivity has a relatively minor effect on net radiative energy balance in the stratosphere. In contrast, since stratospheric temperatures are higher than those in the underlying upper troposphere, an increase in emissivity leads to an overall increase in LW emission. As a result, enhanced LW emission exceeds absorption, leading to net radiative cooling in the stratosphere following an increase of WV (30, 31). Conversely, stratospheric aerosols efficiently scatter visible light but strongly absorb near-infrared radiation. Based on extensive measurements conducted after the 1991 Mt. Pinatubo eruption, volcanic sulfate aerosols were found to induce net radiative warming in the stratosphere (2). Following the HT eruption, a pronounced negative temperature anomaly of up to -4K was observed in the mid-stratosphere over the low-latitude regions of the Southern Hemisphere persisting for more than a year (22, 24, 32, 33). This anomaly is hypothesized to indicate net radiative cooling after the HT eruption, primarily driven by WV enhancement (24, 34). Although the heating effect of volcanic aerosols is hard to discern from negative temperature anomaly observations, the relative contributions of WV and aerosols to these temperature changes over time after the eruption remain to be fully quantified, especially considering the impact of stratospheric circulation change (highlighted in red in Fig. S1 of the supplement). On the other hand, in addition to direct radiative cooling, enhanced stratospheric WV is also hypothesized to accelerate the SO_2 oxidation to form

sulfate particles (29) and hydrate the stratosphere, promoting particle hygroscopic growth (highlighted in pink in Fig. S1). Both processes may enhance the aerosol radiative effect of warming. However, this indirect role of WV in temperature perturbation via aerosol processes is still not well understood. Using satellite observations, this attribution study develops analytical models to elucidate the contributions of different processes to the rapid growth of aerosol particle size, some of which are influenced by enhanced WV. Subsequently, the relative roles of large volcanic aerosols and WV in modulating stratospheric temperature after the HT eruption are quantified. This two-stage analysis reveals the disparate roles of WV in perturbing the stratospheric thermal structure over time and altitude, leading to a comprehensive understanding of the net radiative effects associated with WV and various aerosol formation processes after the HT eruption, as highlighted in Fig. S1.

Results

HT gas injection

As illustrated in (17), before its most powerful explosion on 15 January, HT had been having early eruptions and SO_2 emissions since late December 2021. These early SO_2 plumes were identified using the lower stratospheric SO_2 column density (referred to as STL SO_2) observed by the OMPS Nadir-Mapper (NM) regardless of their injection altitudes (e.g., upper troposphere on 22 December or stratosphere on 15 January, Fig. 1A). In contrast, MLS detected a significant stratospheric SO_2 mass anomaly only after 15 January (Fig. 1C). Nevertheless, the estimated stratospheric SO_2 e-folding decay time of ~7 days after the HT eruption from MLS observations is comparable to the ~6-day estimate from OMPS-NM (17). This indicates that the impact of early eruptions on stratospheric SO_2 perturbations and subsequent sulfate particle formation is negligible and, therefore, not further investigated in this study.

In contrast to the small amount of SO_2 emitted was the huge amount of WV injection from HT and its new reach in altitude (21-24). HT's WV injection of 150-160 Tg, shown in Fig. 1C, (18, 23), was comparable to, even more than that (75-150 Tg WV) speculated for the 1991 Mt. Pinatubo eruption (28, 37), whereas its SO_2 emission was 10-100 times smaller than that (12-20 Tg, (38)) of the Mt. Pinatubo eruption. The formation of volcanic sulfate particles starts from the oxidation of SO_2 by the OH radical, which could be enriched by simultaneous WV injection. However, the oxidation rate depends not only on the total amount of WV injected but also its injection profile in the stratosphere. WV injected at lower altitudes with lower temperatures (e.g., just above the tropopause) can form more ice and quickly sediment (37, 39). Therefore, although ice formation from HT injected WV was also inferred as in (29), the lower injection height of WV during the Pinatubo eruption (18-25 km) (37, 40, 41) compared to that of the HT eruption (40-50 km) likely resulted in a greater fraction of the injected water freezing and more sedimentation as ice crystals following the Pinatubo event. Consequently, the amount of WV available for SO_2 oxidation was reduced (e.g., ~1/3 amount from model simulation in (37) with a 25 km injection height). The crucial role of WV in accelerating the SO_2 oxidation rate by providing more OH radicals after the HT eruption was highlighted by the prolonged SO_2 e-folding time from simulations without WV injection in (29). Consequently, although the volcanic ash injected by the Pinatubo eruption could accelerate the SO_2 oxidation by 10 %–20 % (37), the satellite observed SO_2 e-folding decay time after Pinatubo (35 days) (40) was longer than that after the HT eruption (6-7 days). This reveals a notably faster rate of SO_2 oxidation after the HT eruption contingent upon the amount of WV retained in the stratosphere, which in turns is determined by both the high injection height and the large total amount of WV injection. Furthermore, while this WV plume initially dispersed vertically within the 1-100 hPa range

immediately after the eruption (Fig. 1B), an enhanced WV layer persisted at 20-30 hPa for over a year, perturbing temperature in that region, which was analyzed in later investigations.

Observed stratospheric aerosol evolution after HT

While previous studies have analyzed the evolution of stratospheric aerosol extinction and particle size profiles after the HT eruption using observations from the Ozone Mapping and Profiling Suite Limb-Profiler (OMPS-LP) and the Stratospheric Aerosol and Gas Experiment III aboard the International Space Station (SAGE III/ISS), this study further elucidates the correlation between extinction and particle size with a particular emphasis on their distinct vertical distribution compared to WV anomaly profiles. The peak aerosol extinction enhanced by the HT eruption was observed at an altitude of ~22-24 km starting in February and gradually descended to 20-22 km by the end of 2022 (23). At these altitudes, the extinction was ~ten times larger than the background value in the tropics and subtropics (20˚N-30˚S) and more than twice as strong as those associated with other volcanic eruptions and major wildfire events since 2014 (Fig. 2B). However, this layer where aerosol extinction peaks was lower than the enhanced WV layer, which persisted for over a year at 20–30 hPa (~24–26 km) after the initial dispersion of the HT plume, as captured by MLS (Figs. 1B and S3). The displacement of peak altitudes between aerosol and WV underscores the need to investigate how enhanced WV and aerosols modulate stratospheric temperature at different altitudes. Furthermore, the Angstrom exponent (AE), representing the wavelength dependence of aerosol extinction derived from the multi-channel measurements of OMPS-LP (and SAGE III/ISS) is regarded as an indicator of sulfate particle size. The evolution of the altitude and latitude of low AE, indicative of large particle sizes, was consistent with the distribution of strong aerosol extinction, not only in the subtropics but also in the mid-latitudes (Fig. 2A). Particularly, the high negative correlation between β_{997} and AE (R < -0.8) reveals that the large sulfate particle size was the dominant factor causing strong aerosol extinction. Since the emission of SO_2 was limited, the increase of aerosol extinction did not directly reflect a proportional increase in sulfate (SO_4) mass, but was more likely caused by particle growth. The presence of unusually large particles in the lower to middle stratosphere resulted in the detection of the lowest AE in the past ten years in the tropics and subtropics from OMPS-LP (20-26 km, Fig. 2B), which led to larger particle surface area density and influenced heterogeneous reactions in stratospheric chemistry (44). The distribution of low AE also matched the descent of the aerosol layer (Fig. 2B), indicating it was mainly caused by the gravitationally settling down of large particles (24). From a global perspective, the SAGE III/ISS observed global mean AE kept decreasing for at least a year after the HT eruption. This contrasts with the rapid drop and return after 2019 Raikoke and Ulawun eruption, indicating the long-term impact of large HT volcanic sulfate particles in global stratospheric aerosols (Fig. 2C).

By combining satellite-observed AE with aerosol extinction, we derived profiles of effective radius (R_{eff}), aerosol volume concentration (V), and aerosol number density (N) (see Methods, with the assumption of sulfate particles dominated by sulfuric acid droplets (H_2SO_4-H_2O) following single-mode lognormal size distribution with geometric standard deviation σ of 1.6). Focusing on the HT volcanic aerosols source region (0˚-30˚S), the SAGE III monthly R_{eff} reached its largest value of ~0.35 μm at 22-24 km in March 2022 (Fig. 3A); this was larger than the background of 0.1-0.2 μm and smaller than the counterpart of 0.5-0.6 μm after the Pinatubo eruption (45, 46). Indeed, the global mean stratospheric aerosol optical depth (SAOD) after HT reached 0.02 (at 520 nm), much lower than that of ~0.15 (at 550 nm) associated with the Pinatubo eruption (Fig. 2C, (47, 48)). However, the rate of particle size growth during the first two months after the eruption was similar between these two eruptions (46). Comparing measurements from different satellites, AE from OMPS-LP was always lower than that from SAGE III/ISS for either background or volcanic aerosols, indicating that they have systematic differences (Fig. S5B). As a result, the peak R_{eff} derived from OMPS-LP was 0.45-0.5 μm, 0.05-0.15 μm larger than that from SAGE III/ISS. As mentioned in Methods, R_{eff}, V, and N retrievals from satellite observations depend on the assumption of σ or spread in the particle size distribution. With σ varying between 1.4 to 1.8 (45), R_{eff} displays an uncertainty of 2%-8% (0.009-0.026 μm); this uncertainty for large R_{eff} (> 0.4 μm) can be ignored (< 0.016 μm), similar to a 7-8% uncertainty in V (Fig. 3A and 3B). Although different

σ values may cause large uncertainty in N retrieval (Fig. 3C), it has little impact on our attribution analysis of different microphysical processes in aerosol evolution, as described in the following section. Note that the AE calculation in this study was based on a wavelength pair of 675 and 997 nm for OMPS-LP, comparable to the 676-1021 nm pair used for SAGE III/ISS. However, variations in wavelength pairs, such as 384-1540 nm from SAGE III/ISS in (23), 355-532 nm from lidar observation in (49) or the three wavelengths (449, 755 and 1543 nm) used by (50), can lead to differences in R_{eff} ranging from ~0.4 to 0.6 μm, even under the same assumption of a unimodal lognormal size distribution. Additionally, assuming a bimodal size distribution could also cause a R_{eff} difference of less than 0.1 μm (7). In situ balloon measurements and gravitational settling rates calculated from satellite measurements further reveal the presence of large volcanic sulfate particles with radii exceeding 0.5 μm (24, 43, 51). These findings underscore the importance of exploring the primary factors driving the growth of HT volcanic sulfate particles, particularly the significant role played by the large amount of WV injected during the HT eruption.

Aerosol microphysical processes contributions to particle size growth

We developed an analytical model containing a series of ordinary differential equations (ODEs) describing R_{eff}, V, and N variation with time (see Methods) to isolate the individual contributions of different microphysical processes to the particle evolution after the HT eruption. Processes considered include nucleation, coagulation, condensation, hygroscopic growth, and transport (loss processes, including sedimentation and evaporation, are represented collectively). While past studies have hypothesized that coagulation could have significantly caused sulfate particles to grow (29, 43), a quantitative analysis of the relative roles of these processes in particle size evolution has not been made. Particularly, as WV injection from the HT eruption enhanced stratospheric moisture content, the role of WV concentration or relative humidity (RH) that determines hygroscopic growth was quantified here. Note that "condensation" refers to the condensation of H_2SO_4 vapor on the particle surface.

The analytical ODE model with the constraints of OMPS-LP observations enabled us to attribute the relative importance of each process to R_{eff}, V, and N evolution (Figs. 4A and 4B). For example, during the first 10 days after the HT eruption, at the altitude of 23.5 km where R_{eff} and β_{997} values were the largest, our model quantitively shows that although coagulation reduced N by 20-30%, nucleation dominated N evolution and caused 70-80% of the observed growth of N (Fig. 4A). Consequently, N increased rapidly by a factor of 4 from (1.5 ± 1.3) cm^{-3} to ~(7 ± 5.4) cm^{-3} (median value $\pm$ standard deviation for different σ, hereafter) during those 10 days, illustrating the rapid nucleation of new particles from H_2SO_4 vapor. Our model also shows that condensation explained nearly 100% of the increase in V. Indeed, the volume increase due to nucleation was negligible because the small size of new particles and coagulation due to Brownian motion would not change particle volume concentration. Another reason is that daily mean relative humidity with respect to water (RH) increased by 2-6% due to HT WV emission. In spite of a large increase compared to less than 1% RH in the background stratosphere, R_{eff} increased by only 0.02-0.04 μm and had limited impact on the change of V based on the thermodynamics and parameterization of hygroscopic growth (see Methods and Fig. S9). Overall, nucleation reduced R_{eff} by adding small particles, while condensation and coagulation caused particle size growth; together, they resulted in a slow increase in observed R_{eff}, demonstrating the persistence of the contribution from condensation and coagulation over these 10 days.

Starting in late January, N decreased quickly as a result of the increasing contribution ($46 \pm 2.3\%$) of coagulation and the decreasing contribution ($53 \pm 2.3\%$) of nucleation, as found in our model (Fig. 4A, red lines). With more impact factors, the changes in R_{eff} (with respect to the background value, i.e., no process is considered) contributed from each single process during the whole year from our model were shown as the filled areas in Fig. 4B. Condensation dominated particle size growth, resulting in > 60% of the total variance of particle size when the observed R_{eff} increased; the remaining 30-40% was due to the particle size increasing by coagulation (7-14%) and decreasing by nucleation (23-25%), respectively. Eventually, R_{eff} and V increased with a growth

rate assuming e-folding decay of ~20 days. The assumption of different σ used in the retrievals and ODE model can cause a 1-3% (0.2% for hygroscopic growth) variance in contribution for each process (see details in the supplementary Text S4). In essence, the size growth of HT aerosols was controlled by the gas-to-particle conversion, including condensation and nucleation (~90%), the rate of which relies on the concentration of H_2SO_4 vapor produced from SO_2 oxidation. Based on the nucleation rates derived from our ODE fitting and their dependence on H_2SO_4 vapor and RH (52), the H_2SO_4 vapor concentration ranged from ~10^6 to 10^8 cm^{-3} in the first two months after the HT eruption, which was comparable to the simulations of H_2SO_4 following the Pinatubo eruption (~10^6 to 10^7 cm^{-3}) reported in (53) and a recent simulation (~10^7 cm^{-3}) for HT aerosols (54) from a microphysical model (Fig. 4C, see details in supplementary Text S6). We noted, however, that H_2SO_4 was a transit state in the gas-to-particle conversion process. These results agree with the hypothesis that despite the low SO_2 emissions from the HT eruption, the SO_2 oxidation rate was accelerated by the high OH concentration from abundant HT WV emissions, thereby leading to a shorter lifetime of SO_2 (29) and H_2SO_4 vapor production comparable to that after the Pinatubo eruption. Consequently, the fast production of H_2SO_4 vapor led to fast particle size growth, indicating the significant role of WV emission in large HT particle formation. Future studies can further compare the ODE model with other models and observations for different volcanic eruptions.

What limited the growth of particle size after HT eruption, as compared to that of the Pinatubo eruption, was the smaller amount of SO_2 emitted. As a result, the presence of the large particles at the high altitude of 22-24 km persisted for less than three months before the sedimentation and transport process started to dominate in May. Subsequently, R_{eff} and V decayed quickly, while N remained nearly unchanged (with only a slight decrease), reflecting the loss of large particles from sedimentation, evaporation, and transport; these processes collectively led to a loss rate (e-folding decay) of ~29 days. The presence of these large particles could increase the particle surface area density (for the same particle number), thereby enhancing the heterogeneous chemical reactions associated with ozone depletion (55-57). Actually, the observed ozone depletion within the HT volcanic plume (58) has been attributed to the increased surface area density identified as a key factor for enhancing heterogeneous reactions while other factors, such as the temperature decrease and relative humidity increase also played significant roles (59). However, as reported in (44), the moderate enhancements in reactive chlorine in the southern mid- and low-latitude stratosphere, associated with heterogeneous processing on HT volcanic sulfate, did not cause appreciable chemical ozone loss.

Disparate roles of WV and aerosols in the stratospheric temperature perturbation

The large amount of WV is expected to lead to cooling in the stratosphere. However, its effect on the enhancement of aerosol particle growth and aerosol extinction could also result in significant stratospheric warming from aerosols. From satellite data, in the middle stratosphere (e.g. 21 hPa, ~26 km) where both WV and aerosol extinction enhancement existed, the temperature showed a large negative anomaly (ΔT) of -4 K for 4-7 months in the subtropics, and reached -8 K in the mid-latitudes (Fig. 5B, (24, 33, 34)), whereas only a small positive anomaly was found in the subtropical lower stratosphere (Fig. 5A, (60)). The stratospheric cooling after the HT eruption was indeed the coolest period in the mid-latitudes since 1994 (Fig. S12).

We used a first-order multi-variable linear regression model to quantify the influence of local volcanic aerosols, WV, and stratospheric dynamics changes (manifested as the anomaly of a tracer, N_2O) on temperature anomaly (see Methods). At 21 hPa, where WV enhancement persisted for over a year, assuming a ~1 month response time for temperature, which rendered the robust regression with the strongest correlation and lowest residual between fitted and observed ΔT (details in Methods), we found that in the subtropics, the partial ΔT associated with the WV anomaly displayed a trend similar to the MLS-observed ΔT, indicating that the WV enhancement largely accounted for the negative temperature anomaly over the following 7-month period (green lines). Conversely, the negligible aerosol-induced ΔT (blue lines) suggested that despite an increase in aerosol extinction at this altitude, this enhancement was insufficient to substantially heat the

stratosphere as observed in other major volcanic eruptions (61-63). This regression analysis further confirmed the near-zero aerosol-induced heating rate reported by (34), as well as the one order of magnitude smaller heating rate from enhanced aerosols compared to the enhanced WV after the HT eruption, which we estimated from the Fu-Liou radiative transfer model (Fig. 5D, see details in the supplementary Text S7). In contrast, WV cooling played the predominant role, contributing to over 60% of the ΔT, while the dynamics anomaly described by the N_2O tracer offset up to 10% of the WV cooling effect, restoring the temperature to normal levels after October 2022 (Figs. 5B and 5C). However, in lower stratosphere, such as at 100 hPa, where aerosol extinction was enhanced not only soon after HT eruption due to the formation of volcanic particles but also after a few-month transport of these particles (since May) likely due to the sedimentation of large particles from upper layers (such as at 22-24 km), the aerosols' warming effect accounted for over 50% of the stratospheric ΔT. WV displayed few perturbations after the HT eruption, suggesting a negligible effect of the WV cooling (Fig. 5C). Compared with mid-stratospheric cooling of up to -4 K, the lower stratospheric warming with an amplitude of ~1-2 K was much smaller. This warming became more pronounced after July when the sedimentation became discernible from aerosol extinction variation, which underscores the disparate (and indirect) role of WV in affecting stratospheric thermal structure via the processes to form large particles (Fig. 5A and 5B). At mid-latitudes, where both aerosol and WV enhancement were due to the transport from low-latitudes, WV cooling had a dominant (40%-80%) contribution to the temperature change. Dynamics changes led to only a small perturbation of temperature (5%-20%) and aerosol radiative effect can be ignored (Fig. 5C). Note that in the lower stratosphere at mid-latitudes (100 hPa), the observed small ΔT may not be explained primarily by the local effect from HT volcanic aerosols, WV injection, and dynamics change (Fig. S13).

Henceforth, the notable negative temperature anomaly observed within 12 months after the HT eruption reflected the predominant role of the WV cooling effect on the middle stratospheric temperature variation, which also partly responded to the circulation anomalies. The radiative effect of volcanic aerosols was negligible, aligning with radiative forcing estimates from radiative transfer models (24, 33, 34). In contrast, the absence of WV enhancement in the lower stratosphere suggests that the smaller temperature perturbation observed at these levels was likely dominated by aerosol-induced warming. This effect became more pronounced as aerosol plume descended through sedimentation and was transported in approximately half a year after the HT eruption. The disparate radiative impacts of WV and aerosol plume, along with their vertical separation, such as the gravitational settling of large particles whose formation was promoted by WV, agree with the observation of opposing temperature anomalies in the lower and middle stratosphere, highlighting their respective roles in driving stratospheric temperature perturbations at different altitudes. On the other hand, only the correlation between the observed temperature anomaly and localized WV and aerosols radiative effects were analyzed here. The influence of WV and aerosols in other layers was hard to quantify using a regression model and not discussed in this study.

Discussion

With the constraints of multiple satellite observations, first-order analytical models were developed and used to show the unusual role of WV in the evolution of aerosol size and number as well as temperature in the lower and middle stratosphere after the HT eruption. Quantitively, we found that fast gas-to-particle conversion including nucleation and condensation dominated particle formation and particle size growth. This solidifies the conjecture that the huge WV emission could accelerate SO_2 oxidation by enriching OH concentration which controls the conversion rate of SO_2 to H_2SO_4, resulting in high H_2SO_4 vapor concentration over a short period and accelerating gas-to-particle conversion. In fact, the H_2SO_4 vapor concentration from our model in this study was comparable to the simulation following the Pinatubo eruption, indicating similar H_2SO_4 production through SO_2 oxidation in the first three months after the HT eruption, despite its lower SO_2 emission. This finding reveals the essential role of abundant WV in the rapid

formation of large sulfate particles, which accounted for the strong aerosol extinction observed after the HT eruption. Overall, these additional large volcanic aerosols after HT eruption could enhance aerosol surface area density in the stratosphere, increasing the rate of heterogeneous chemical reactions that play a role in stratospheric ozone chemistry. In-plume ozone depletion has been observed within days after the HT eruption through balloon-borne measurements (58), which coincided with the negative hydrogen chloride anomalies and positive chlorine monoxide anomalies, ascribed to the heterogeneous chlorine activation on humidified volcanic aerosols (58, 59). However, Santee*, et al.* (44) highlighted that ozone in the southern middle and low-latitude stratosphere remained primarily influenced by transport processes with limited evidence of chemical diminishment. More studies about long-term impact of the HT eruption on stratospheric ozone are still ongoing. Furthermore, although the strong radiative warming is expected from these large volcanic aerosols promoted by WV in the stratosphere, this warming effect cannot offset the total cooling effect from WV in the middle stratosphere, especially in the mid-latitudes. Satellite measurements revealed that the substantial WV emission and relatively modest SO_2 emission from the HT eruption induced a pronounced mid-stratospheric cooling with a quick start, a relatively long duration over a year, and a significant amplitude of -4 K. In contrast, a mild warming of 1-2 K was observed in the lower stratosphere, which became evident after July, and was mainly attributed to the sedimentation of large particles formed at higher altitudes. This phenomenon sharply contrasts with the stratospheric warming typically associated with volcanic eruptions dominated by volcanic sulfate (61). However, the reduction in direct solar flux due to enhanced aerosol extinction remained the dominant factor in the net negative radiative effect at the surface, contributing to the slight surface temperature decrease observed after the HT eruption (64).Therefore, the relative amount of WV and SO_2 emissions, as well as the altitudes of their enhancement, are critical factors for predicting the climate impact of volcanic eruptions.

Methods

Satellite data

In this study, satellite data describing global stratospheric composition and temperature from multiple sensors are analyzed together with the model-based re-analysis data, each of which is introduced as follows.

- The sulfur dioxide (SO_2) and temperature profiles from 100 hPa to 10 hPa, as well as the water vapor (WV or H_2O, gas-phase) profiles from 100-1 hPa of the Microwave Limb Sounder (MLS) onboard the Aura satellite are analyzed in this study (65). MLS onboard NASA's Aura satellite observes thermal microwave emission from Earth's limb, both day and night since 2004. This enables the retrieval of vertical distribution of atmospheric composition, temperature, humidity, and cloud ice above the upper troposphere. The broad spectral bands of MLS facilitate measurements of volume mixing ratios for more than 10 trace gases with vertical resolution of 3 – 5 km and a spatial resolution of ~165 km. The pressure range and quality screening for reliable retrievals varies by gas and are outlined in the user guide (https://mls.jpl.nasa.gov/data/v5-0_data_quality_document.pdf). However, in the first few weeks after HT eruption, the substantial WV enhancement in the upper troposphere and stratosphere of more than an order of magnitude greater than previous observations failed the quality screening criteria (18). Consequently, applying quality control procedures as recommended may have excluded the enhanced WV, leading to a mass anomaly ~10 Tg lower than that from version 4.2 product. Thus, a comparative analysis of the stratospheric WV mass anomaly with the inclusion and exclusion of quality control is presented in Fig. 1C. For the subsequent analysis in this manuscript, the MLS version 5.0 SO_2 and temperature products after filtering low-quality data and the version 4.2 WV product without applying quality control are used. The quality guaranteed N_2O profile measurements used in the regression analysis of temperature anomaly also come from MLS, thereby can only be applied at pressure levels equal or lower than 100 hPa.

- Also used are the Version 2.1 products of stratospheric aerosol optical depth (SAOD) and extinction coefficient profiles at two wavelengths (675 and 997 nm), retrieved from the Ozone Mapping and Profiling Suite (OMPS) Limb-Profiler (LP) on the Suomi-NPP satellite since 2012, in the 0.5-40 km altitude range with 1.8 km vertical resolution (66). Each of OMPS-LP orbit measures three limb profiles spaced approximately 250 km in the cross-track direction. Each profile provides along-track sampling of approximately 125 km. As the aerosol extinction profiles at longer wavelengths have demonstrated superior accuracy and precision in the southern hemisphere (66), we focus on the 997 nm product from all three slits in this study. Note that OMPS-LP 997 nm radiance measurements were only available after 2013 November, so our analysis only includes OMPS-LP data starting from 2014 January. Additionally, a contiguous daily SO_2 product of 50 km resolution from a nadir-viewing hyperspectral instrument measuring 300–380 nm radiance onboard Suomi-NPP, named OMPS-NM was also analyzed. Total vertical SO_2 column amount, retrieved with a prescribed Lower STratospheric (STL) profile centered at 16 km above surface demonstrates the enhanced SO_2 abundance relevant to HT eruption.
- Version 5.20 SAGE III/ISS aerosol extinction profiles at nine wavelengths (384, 449, 521, 602, 676, 756, 869, 1022, and 1544 nm) are analyzed for comparison with OMPS-LP data. Its WV profiles are also analyzed together with MLS data to verify the evolution of WV. SAGE III is a third-generation solar occultation instrument for the Stratospheric Aerosol and Gas Experiment on the International Space Station (ISS) (SAGE III/ISS). It started to measure the stratospheric ozone, water vapor, nitrogen dioxide, and aerosol extinction profiles from the surface to ~100 km in 2017 after the retirement of its last-generation SAGE I and SAGE II. As a result of a well-calibrated occultation technique, SAGE III data have higher accuracy and finer vertical resolution (0.5 km) than those of limb instruments such as OMPS-LP, but with a smaller number of spatial samplings confined within the limited latitude range each day since it only tracked sunrise or sunset events (or lunar events but not applied here) (67).
- Other data, such as the three-dimensional wind vectors from the re-analysis data collection in the Modern-Era Retrospective analysis for Research and Applications version 2 (MERRA-2), are also included in this study to help track the transport of SO_2 plumes from HT eruption.

From the MLS profiles of SO_2 and WV volume mixing ratio (VMR), we derive the masses of SO_2 and WV in the stratosphere, which are then used to estimate their emission from the HT eruption. Following the formula derived by Livesey and Snyder (68) (Appendix A.3), for each MLS pixel, we integrate the MLS VMR vertical profiles from 100 hPa to 10 hPa (or 1 hPa for WV) given the 20-30 km injection altitude of HT eruption to form the corresponding stratospheric column number density (STL, in unit molecules m^{-2}). Subsequently, following the method in (69), the daily mean STL in our domain of interest, defined as -180°~180° longitude and 0°~40°S latitude, is calculated and multiplied by the domain area to get the total daily mean stratospheric gas amount. To extract the enhanced gas concentration associated with volcanic emission from the background in the silent atmosphere, the MLS level 3 monthly binned profile products from 2005 to 2021 are used to fit the background concentration considering its long-term linear trend, annual, semi-annual and quasi-biennial oscillation (QBO) sinusoidal cycles, especially for WV. At each pressure level, a linear combination of these variation terms with different periods is used to fit the regional mean gas VMR observations (as Eq. 1 in (70)). After optimizing the parameters in each term, background gas concentration in 2022 was approximated by this function. Subtracting this background value from MLS observations in 2022, we derived the VMR anomaly due to HT eruption and calculated the mass anomalies shown in Fig. 1B.

Aerosol effective radius (R_{eff}), volume concentration (V), and number density (N) derivation

Since the aerosol extinction coefficients (β_i) from OMPS-LP and SAGE III/ISS are retrieved from multiple channels (ith wavelength), the Angstrom Exponent (AE) can be derived between any paired wavelengths (675 to 997 nm for OMPS-LP and 676 to 1021 nm for SAGE III/ISS). When assuming that volcanic aerosols are dominated by pure sulfuric acid particles with a single-mode

lognormal size distribution (PSD, $\frac{dN(r)}{dr}$) described by two parameters (r_g and σ in Eq. 1), the Mie model enables us to retrieve aerosol effective radius defined as Eq. (2) from satellite-observed AE, as in a previous study (45).

$$\frac{dN(r)}{dr} = \frac{N}{r\ln\sigma\sqrt{2\pi}}\exp\left[-\frac{1}{2}\left(\frac{\ln r - \ln r_g}{\ln\sigma}\right)^2\right] \quad (1)$$

$$R_{\text{eff}} = \int \frac{dN(r)}{dr} r^3 dr \Big/ \int \frac{dN(r)}{dr} r^2 dr = r_g \exp\left[\frac{5}{2}(\ln\sigma)^2\right] \quad (2)$$

In the Mie model, we considered the dependency of the aerosol refractive index on the wavelength. The weight of H_2SO_4 in sulfuric acid particles (Table 1 in (45)) was derived from MLS temperature and WV profiles (71). Generally, from 100 hPa to 10 hPa in the research region, the H_2SO_4 weights (wt %) are 45% to 80%. The HT volcanic aerosols R_{eff}, V, and N are retrieved using the following steps. First, assuming σ of 1.6 (unitless, mean value of volcanic sulfuric acid PSD in (45)), R_{eff} can be retrieved from satellite AE measurement; Second, combing the satellite-observed β_{997} (β_{1021} for SAGE III/ISS) and the retrieved R_{eff}, we derived the aerosol volume concentration (V, m^3/m^3) following Eq. (3),

$$V = \int \frac{4}{3}\pi r^3 \frac{dN(r)}{dr} dr = \frac{4}{3} R_{\text{eff}} \int \pi r^2 \frac{dN(r)}{dr} dr = \frac{4}{3}\frac{\beta_{997} R_{\text{eff}}}{Q_{997}} \quad (3)$$

where Q_{997} is the aerosol extinction efficiency for polydisperse particle populations defined as $Q_{997} = \frac{\int \pi r^2 q_{997}(r)\frac{dN(r)}{dr}dr}{\int \pi r^2 \frac{dN(r)}{dr}dr} = \frac{\beta_{997}}{\int \pi r^2 \frac{dN(r)}{dr}dr}$ (computed with the Mie model). Finally, the particle number density (N, cm^{-3}) is derived using the averaged volume per particle over the PSD ($v_a = \frac{\int \frac{4}{3}\pi r^3 \frac{dN(r)}{dr}dr}{\int \frac{dN(r)}{dr}dr} = \frac{V}{N}$, μm^3 from Mie model) and V. Since the Mie model simulations rely on the assumption of σ value, given the normal range of σ for volcanic sulfuric acid PSD, 1.4 to 1.8 (45), the possible uncertainties of retrieved R_{eff}, N and V due to different values in this range are shown as error bars in Fig. 3B and 3C (the percentage of R_{eff} uncertainty is emphasized as black contour lines in Fig. 3A).

Aerosol hygroscopic growth estimation

When the relative humidity in the surrounding atmosphere increases, sulfate particles could grow by uptaking water on the surface, known as hygroscopic growth. Based on previous studies (72-74), considering the sulfuric acid (or sulfate) solution droplet, the droplet hygroscopic growth factor describing the change in size of droplet in equilibrium with the surrounding humidity is defined as:

$$f = \frac{r}{r_0} = \left(\frac{100}{x}\frac{\rho_0}{\rho}\right)^{1/3} \quad (4)$$

where r_0 is the radius for a dry particle without any water uptakes and r is the radius of a wet particle of density r at x wt % in the air with density r_0. The relative humidity with respect to water (RH, %) can be given by $100a_w$, in which a_w represents the water activity. From experiments in the laboratory, r and a_w can be expressed by polynomials of x, whose coefficients were summarized in Table1 of (73). Thus, the relationship between f and RH can be derived by changing x, as in Fig. S9A. Following this relationship, if there was no volcanic sulfate formation, only RH increasing (from < 1% to 5%) due to HT WV emission can cause f to increase from ~1.03 to 1.15 (Fig. S9). Here, the daily RH profile is averaged in the MLS-observed WV plume with the

maximum VMR larger than 10 ppmv in the altitude of 100 -1 hPa. When applying this growth factor in R_{eff}, an increase in particle size solely via hygroscopic growth is small and mainly remains in the lower stratosphere (< 18 km), which does not match the satellite observations of large particle size located at 22-24 km.

Ordinary differential equation (ODE) system

Since the evolution of R_{eff}, V, and N are determined by multiple microphysical processes, we establish an ordinary differential equation (ODE) system to model the evolution of particle microphysics. To best represent the underlying physical processes, observation-based estimates of R_{eff}, V, and N are used to fit a set of coefficients in the ODE system to minimize the discrepancy between the model and observations. This ODE model is later used to evaluate the contribution of each process to the overall evolution of particle microphysics. Here, five processes are considered: nucleation, coagulation, condensation, hygroscopic growth, and transport. As mentioned in the main text, the "transport" hereafter represents an ensemble particle removal process including gravitational sedimentation, zonal transport, and evaporation during the particle movement. For modeling, we discretized the evolution process at different time steps t_i with equal intervals of Δt (Δt = 1 day for OMPS-LP measurements here), where the subscript i is the number of time steps (days after eruption) (starting from 0 as the initial condition). Consequently, the instantaneous values of R_{eff}, V, and N for each time step t_i can be expressed by the following five equations:

$$N_i = N_{i-1} + (\frac{dN}{dt})_i \Delta t, \tag{5}$$

$$V_i = V_{i-1} + (\frac{dV}{dt})_i \Delta t, \tag{6}$$

$$v_{a,i} = \frac{V_i}{N_i}, \tag{7}$$

$$R_{\mathrm{eff},i} = g(v_{a,i}), \tag{8}$$

$$(\frac{dX}{dt})_i = (\frac{dX}{dt})_{\mathrm{nucleation},i} + (\frac{dX}{dt})_{\mathrm{condensation},i} + (\frac{dX}{dt})_{\mathrm{coagulation},i} + (\frac{dX}{dt})_{\mathrm{hygroscopicity},i} + (\frac{dX}{dt})_{\mathrm{transport},i}; \tag{9}$$

Here, X represents any parameter of R_{eff}, V, and N, and $(\frac{dX}{dt})_{\mathrm{nucleation},i}$ is the variation rate of X due to nucleation between t_{i-1} and t_i, similar to other processes shown in the subscripts. We numerically solve this set of equations and parameterize the $(\frac{dX}{dt})_i$ as follows. Assume that the new particles formed via nucleation have the same radius of 0.01 μm, which is the minimum value considered in PSD in our Mie model simulations (value of r_{min}), so $(\frac{dV}{dt})_{\mathrm{nucleation},i} = \frac{4\pi(0.01)^3}{3} \times (\frac{dN}{dt})_{\mathrm{nucleation},i}$. The coagulation increases the particle radius but does not change the particle volumes concentration, i.e., $(\frac{dV}{dt})_{\mathrm{coagulation},i} = 0$. Based on the theory of Brownian coagulation (75), $(\frac{dN}{dt})_{\mathrm{coagulation},i}$ can be expressed using the coagulation coefficient K assumed as a constant for different particle radius at t_i, i.e., $(\frac{dN}{dt})_{\mathrm{coagulation},i} = -\frac{K_i {N_{i-1}}^2}{2}$. This expression has been applied in identifying the role of coagulation mechanism in post-Pinatubo stratospheric aerosols PSD evolution from solar occultation measurements (76). Since the gravitational sedimentation velocity is fast for large particles, we assume its reduction of N can be ignored (i.e., $(\frac{dN}{dt})_{\mathrm{transport},i} = 0$). The downward removal of particles due to sedimentation can

offset most of the upwelling adding of particles at this level due to circulation based on the velocity estimation during the first month after eruption (see supplementary Text S6), hence, the time t_s when V is the largest ($V(t_s) = \max(V(t))$) is used as a separator for condensation and transport while other processes have little effect, i.e., when $t_i < t_s$, $(\frac{dV}{dt})_{\text{transport},i} = 0$ and when $t_i >= t_s$, $(\frac{dV}{dt})_{\text{condensation},i} = 0$, One of the advantages of this ODE model is to isolate the impact of each process on particle evolution. As shown in Fig. S10, $R_{eff}(t)$ can be simulated for any individual process or any combination of different individual processes. For example, the difference of $R_{eff}(t)$ between considering the condensation and coagulation processes and considering the coagulation process only shows the impact of condensation on $R_{eff}(t)$. At the end, the contribution of each process to $R_{eff}(t)$ is quantified as in Fig. 4B. Similar as above analysis, considering the uncertainties of R_{eff}, N and V from OMPS-LP measurements and the dependency of R_{eff} on v_a from Mie model simulations (g function) caused by σ assumption, the contribution of each process for σ of 1.4 to 1.8 is generated using this ODE system and summarized in the supplementary Table S2. Thus, the uncertainty of this attribution analysis for multiple microphysical processes due to different σ values is concluded.

We incorporated an evaluation of sulfuric acid (H_2SO_4) vapor concentration derived from the nucleation rate estimated by our ODE model, employing the classical binary homogeneous nucleation theory of H_2SO_4 and water (77), along with an improved parameterization outlined in Vehkamäki*, et al.* (52), as shown in Fig. 4C. The parameterized formulas are applicable within the temperature range of 230.15 K to 305.15 K, RH between 0.01% and 100%, and H_2SO_4 concentrations ranging from 10^4 to 10^{11} cm^{-3}. They enable extrapolation of classical results down to 190 K, suitable for the stratospheric conditions.

The multi-variable linear regression of temperature anomaly

To analyze the perturbation of the stratospheric thermal structure after HT eruption, both monthly and daily zonal mean MLS temperature profiles from 2005 to 2022 are used. The multi-year temperature anomaly (ΔT, 2005-2021) is derived from monthly data after removing the seasonal variation. Fig. S11B shows de-seasonalized daily ΔT since 1 December 2021. To remove the long-term trend during these years, a linear regression is fitted from the ΔT profiles, and the regression results are further subtracted from the time series of ΔT. The residual of ΔT following HT eruption is primarily attributed to dynamics perturbations such as circulation anomalies and radiative impacts arising from the atmospheric composition anomaly, e.g., aerosols and WV. As a long-lived species in the troposphere and lower stratosphere, nitrous oxide (N_2O) maintains stable sources from the Earth's surface, with volcanic eruptions exerting no discernible impact on its emission. Therefore, N_2O anomaly (MLS v5.0) after HT eruption primarily reflects changes in stratospheric dynamics and here serves as a tracer for the stratospheric circulation processes anomalies, including the variations in the Brewer-Dobson circulation and the influence of QBO secondary circulation, as established in previous studies (78-81). Further discussion about circulation changes after HT eruption represented by N_2O anomaly is in the supplementary Text S8. Ultimately, the temperature anomaly ΔT after HT eruption is primarily dominated by the radiative effects from enhanced aerosols and WV, which depend on the anomalies of aerosol extinction and WV VMR, as well as the circulation perturbations indicated by N_2O VMR anomaly. Assuming ΔT can be linearly parameterized by these three factors ($\Delta\beta_{997}$, ΔWV and ΔN_2O) in 2022, ΔT can be estimated as in Eq. (10) below:

$$\Delta T = a\Delta WV + b\Delta\beta_{997} + c\Delta N_2O + d. \quad (10)$$

Given the local cooling or warming effect from WV or aerosols, $a < 0$ and $b > 0$ are used as bound constraints in the fitting using the trust region reflective optimization method. Considering the potential response time of temperature to the radiative impact of atmospheric composition perturbations, we tested response times ranging from 0 to 60 days after the eruption. The optimal response time at each pressure level and zonal latitude grid was determined to render the largest correlation coefficients and lowest residuals between ΔT_f fitted from regression model (using

585 ΔWV, $\Delta\beta_{997}$ and ΔN_2O as inputs) and ΔT_o from MLS observations. Fig. S14 shows an example of the variation in correlation coefficient (R) and daily averaged absolute residual (δT = mean($|\Delta T_f - \Delta T_o|$)) with response time at 21 hPa and at 20˚S. For this level, the optimal response time is approximately 1 month. The partial ΔT caused by each factor is quantified by each term in the right side of Eq. (10), shown as dashed lines in Figs. 5A and 5B, indicating the local radiative
590 effect. It is worth noting that the non-zero term d in Eq. (10) at most altitudes (Fig. S14C), which includes effects from other potential factors (e.g. radiative impact from disturbed WV in above layers), indicates that the local radiative effects of enhanced aerosols and WV, along with the circulation processes perturbations expressed as N_2O anomaly, cannot fully account for the observed ΔT. However, the strong correlation between reconstructed and observed ΔT still
595 demonstrates the dominance of these three local factors, particularly the local WV cooling, in the variation of ΔT after HT eruption. Our conclusion aligns with other studies based on radiative forcing estimation from models (24, 34). Similarly, the percentage contribution of each factor to ΔT is estimated as the ratio between the absolute value of each partial ΔT and their sum (Fig. 5C).

600

Heating rate estimations from radiative transfer model

To validate our regression analysis based on satellite measurements, we incorporated the radiative forcing and heating rate estimations from a one-dimensional radiative transfer model (1D Fu-Liou model) attributable to enhanced WV or aerosols due to HT eruption. We utilized a
605 wavelength-dependent refractive index of sulfuric acid from Palmer and Williams (82) assuming 75% H_2SO_4 weight as in Stenchikov*, et al.* (83), along with effective radius (R_{eff}) derived from OMPS-LP, in the Mie model to estimate the single-scattering properties of sulfuric acid from ultraviolet to LW for various particle sizes. These properties, in conjunction with observed aerosol extinction profiles from OMPS-LP, were implemented into the 1D Fu-Liou model to estimate the
610 stratospheric heating rate caused by enhanced sulfate aerosols after HT eruption. Two WV profiles representing the background stratospheric humidity (WV_0) and wetter stratosphere after HT eruption (WV_{HT}) from MLS measurements were utilized (Fig. S13C). Note that we not only estimated the heating rate from enhanced stratospheric WV after HT eruption, but also compared the HT aerosol heating rates under varying WV concentrations (Fig. 5D). The concentrations of
615 other trace gases in the stratosphere, including O_3, N_2O and CO_2 were fixed as the U.S. standard atmosphere.

Data and code availability

620

All satellite data (OMPS-NM, OMPS-LP, SAGE III/ISS, and MLS) were downloaded from NASA Earthdata (https://www.earthdata.nasa.gov) and are free to the public. The version, periods, and details about usage of these data in this study are available in the Methods. The sulfate effective radius, volume concentration and number density retrieved from OMPS-LP and SAGE III/ISS
625 aerosol extinction profiles, as well as the look-up-table derived by Mie code assuming pure sulfuric acid particles can be accessed at Zenodo https://doi.org/10.5281/zenodo.8076397. The Python codes used for data analysis and establishing the ODE model are archived at Zenodo https://doi.org/10.5281/zenodo.8076406.

630 **Acknowledgments**

This work was supported by the funding from National Aeronautics and Space Administration (NASA), Stratospheric Aerosol and Gas Experiment III/International Space Station program (SAGE III/ISS, Grant No. 80NSSC21K1199). We acknowledge the NASA satellite missions,
635 including the OMPS, SAGE III/ISS, and MLS teams, for providing stratospheric gases and aerosol products and the Global Modeling and Assimilation Office (GMAO) for providing the Modern-Era Retrospective analysis for Research and Applications, Version 2 (MERRA-2) data. We also thank S. Solomon of the Massachusetts Institute of Technology for her comments and

P.A. Newman, L. Coy, and S. Pawson of NASA Goddard Space Flight Center for sharing visualization of MERRA-2 data.

Author Contributions

Conceptualization: XC, JW, LJ, LO; Methodology: XC, JW, LJ, MZ, GT; Investigation: XC, JW, LJ, LO; Visualization: XC, ZL; Writing – original draft: XC; Writing – review & editing: JW, MZ, LJ

Competing Interest Statement

The authors declare that they have no competing interests.

References

1. A. Robock, K. E. Taylor, G. L. Stenchikov, Y. Liu, GCM evaluation of a mechanism for El Niño triggering by the El Chichón ash cloud. *Geophysical Research Letters* **22**, 2369-2372 (1995).
2. A. Robock, Volcanic eruptions and climate. *Reviews of Geophysics* **38**, 191-219 (2000).
3. S. Ramachandran, V. Ramaswamy, G. L. Stenchikov, A. Robock, Radiative impact of the Mount Pinatubo volcanic eruption: Lower stratospheric response. *Journal of Geophysical Research: Atmospheres* **105**, 24409-24429 (2000).
4. A. Robock, The climatic aftermath.(Perspectives: Pinatubo eruption). *Science* **295**, 1242-1245 (2002).
5. A. E. Crafford, E. Venzke, eds. (2022) Global Volcanism Program, 2022. Report on Hunga Tonga-Hunga Ha'apai (Tonga) in *Bulletin of the Global Volcanism Network* (Smithsonian Institution).
6. J. L. Carr, Á. Horváth, D. L. Wu, M. D. Friberg, Stereo Plume Height and Motion Retrievals for the Record‐Setting Hunga Tonga‐Hunga Ha'apai Eruption of 15 January 2022. *Geophysical Research Letters* **49** (2022).
7. G. Taha *et al.*, Tracking the 2022 Hunga Tonga-Hunga Ha'apai Aerosol Cloud in the Upper and Middle Stratosphere Using Space-Based Observations. *Geophysical Research Letters* **49**, e2022GL100091 (2022).
8. S. R. Proud, A. T. Prata, S. Schmauß, The January 2022 eruption of Hunga Tonga-Hunga Ha'apai volcano reached the mesosphere. *Science* **378**, 554-557 (2022).
9. W. Zhao, C. Sun, Z. Guo, Reawaking of Tonga volcano. *Innovation (Camb)* **3**, 100218 (2022).
10. A. Amores *et al.*, Numerical Simulation of Atmospheric Lamb Waves Generated by the 2022 Hunga‐Tonga Volcanic Eruption. *Geophysical Research Letters* **49**, e2022GL098240 (2022).
11. R. S. Matoza *et al.*, Atmospheric waves and global seismoacoustic observations of the January 2022 Hunga eruption, Tonga. *Science* **377**, 95-100 (2022).
12. M. Carvajal, I. Sepúlveda, A. Gubler, R. Garreaud, Worldwide signature of the 2022 Tonga volcanic tsunami. *Geophysical Research Letters* **49**, e2022GL098153 (2022).

13. T. Kubota, T. Saito, K. Nishida, Global fast-traveling tsunamis driven by atmospheric Lamb waves on the 2022 Tonga eruption. *Science* **377**, 91-94 (2022).
14. P. Lynett *et al.*, Diverse tsunamigenesis triggered by the Hunga Tonga-Hunga Ha'apai eruption. *Nature* **609**, 728-733 (2022).
15. D. R. Themens *et al.*, Global propagation of ionospheric disturbances associated with the 2022 Tonga Volcanic Eruption. *Geophysical Research Letters* **49**, e2022GL098158 (2022).
16. C. J. Wright *et al.*, Surface-to-space atmospheric waves from Hunga Tonga-Hunga Ha'apai eruption. *Nature* **609**, 741-746 (2022).
17. S. A. Carn, N. A. Krotkov, B. L. Fisher, C. Li, Out of the blue: Volcanic SO2 emissions during the 2021–2022 eruptions of Hunga Tonga—Hunga Ha'apai (Tonga). *Frontiers in Earth Science* **10** (2022).
18. L. Millan *et al.*, The Hunga Tonga-Hunga Ha'apai Hydration of the Stratosphere. *Geophys Res Lett* **49**, e2022GL099381 (2022).
19. M. Zuo *et al.*, Volcanoes and Climate: Sizing up the Impact of the Recent Hunga Tonga-Hunga Ha'apai Volcanic Eruption from a Historical Perspective. *Advances in Atmospheric Sciences* 10.1007/s00376-022-2034-1 (2022).
20. P. Sellitto *et al.*, Observing the SO2 and Sulfate Aerosol Plumes From the 2022 Hunga Eruption With the Infrared Atmospheric Sounding Interferometer (IASI). *Geophysical Research Letters* **51** (2024).
21. J. Xu, D. Li, Z. Bai, M. Tao, J. Bian, Large Amounts of Water Vapor Were Injected into the Stratosphere by the Hunga Tonga-Hunga Ha'apai Volcano Eruption. *Atmosphere* **13**, 912 (2022).
22. H. Vömel, S. Evan, M. Tully, Water vapor injection into the stratosphere by Hunga Tonga-Hunga Ha'apai. *Science* **377**, 1444-1447 (2022).
23. S. Khaykin *et al.*, Global perturbation of stratospheric water and aerosol burden by Hunga eruption. *Communications Earth & Environment* **3** (2022).
24. M. R. Schoeberl *et al.*, Analysis and Impact of the Hunga Tonga‐Hunga Ha'apai Stratospheric Water Vapor Plume. *Geophysical Research Letters* **49** (2022).
25. S. Carey, H. Sigurdsson, C. Mandeville, S. Bronto, Pyroclastic flows and surges over water: an example from the 1883 Krakatau eruption. *Bulletin of Volcanology* **57**, 493-511 (1996).
26. A. W. Woods, K. Wohletz, Dimensions and dynamics of co-ignimbrite eruption columns. *Nature* **350**, 225-227 (1991).
27. S. b. Dartevelle, G. r. G. J. Ernst, J. Stix, A. Bernard, Origin of the Mount Pinatubo climactic eruption cloud: Implications for volcanic hazards and atmospheric impacts. *Geology* **30**, 663-666 (2002).
28. M. M. Joshi, G. S. Jones, The climatic effects of the direct injection of water vapour into the stratosphere by large volcanic eruptions. *Atmos. Chem. Phys.* **9**, 6109-6118 (2009).
29. Y. Zhu *et al.*, Perturbations in stratospheric aerosol evolution due to the water-rich plume of the 2022 Hunga-Tonga eruption. *Communications Earth & Environment* **3**, 248 (2022).

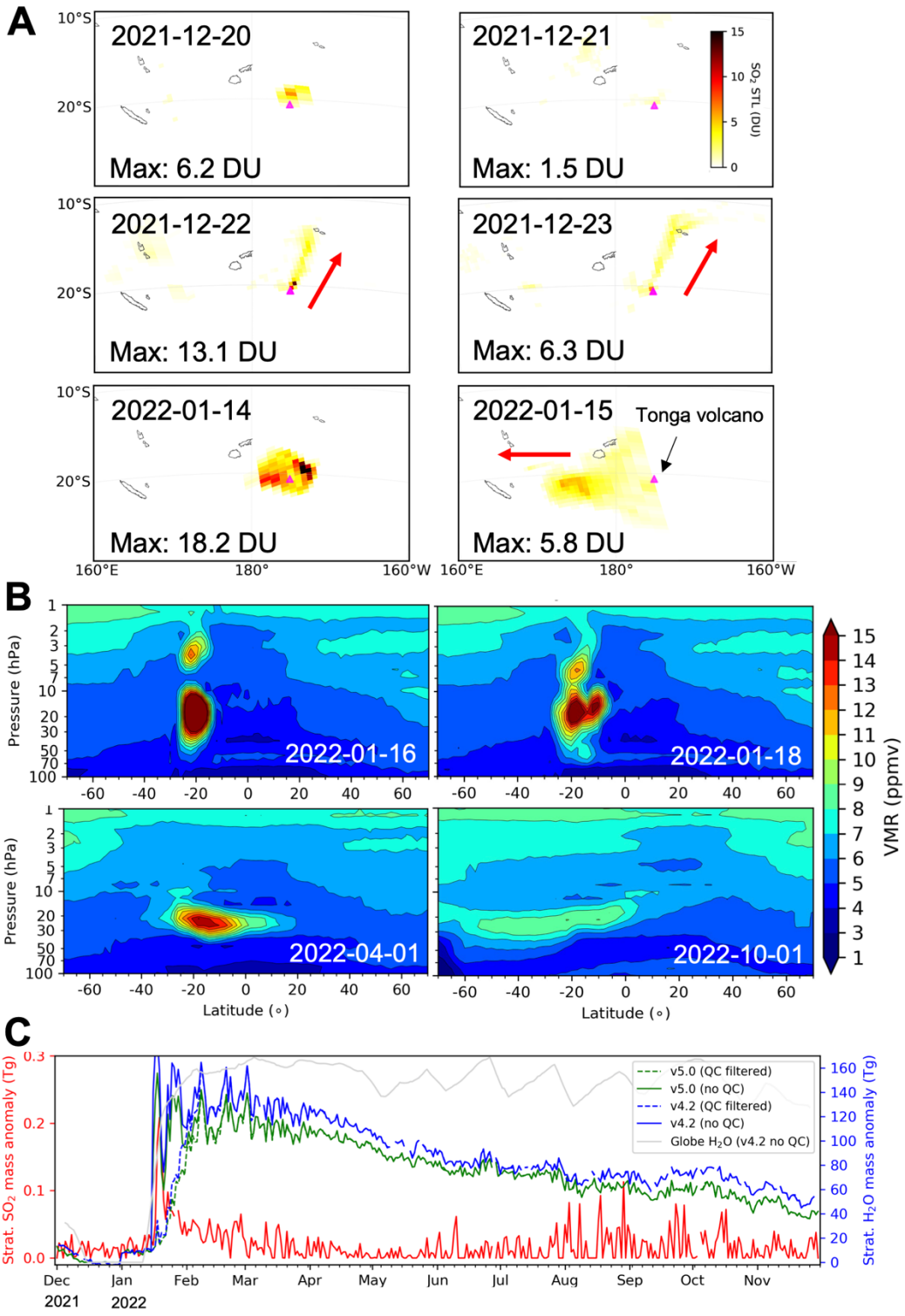
30. D. Rind, P. Lonergan, Modeled impacts of stratospheric ozone and water vapor perturbations with implications for high‐speed civil transport aircraft. *Journal of Geophysical Research: Atmospheres* **100**, 7381-7396 (1995).
31. P. M. d. F. Forster, K. P. Shine, Stratospheric water vapour changes as a possible contributor to observed stratospheric cooling. *Geophysical Research Letters* **26**, 3309-3312 (1999).
32. X. Wang *et al.*, Stratospheric Climate Anomalies and Ozone Loss Caused by the Hunga Tonga‐Hunga Ha'apai Volcanic Eruption. *Journal of Geophysical Research: Atmospheres* **128** (2023).
33. L. Coy *et al.*, Stratospheric Circulation Changes Associated With the Hunga Tonga‐Hunga Ha'apai Eruption. *Geophysical Research Letters* **49** (2022).
34. P. Sellitto *et al.*, The unexpected radiative impact of the Hunga Tonga eruption of 15th January 2022. *Communications Earth & Environment* **3** (2022).
35. A. K. Gupta, R. Bennartz, K. E. Fauria, T. Mittal, Eruption chronology of the December 2021 to January 2022 Hunga Tonga-Hunga Ha'apai eruption sequence. *Communications Earth & Environment* **3** (2022).
36. U. Niemeier, S. Wallis, C. Timmreck, T. van Pham, C. von Savigny, How the Hunga Tonga—Hunga Ha'apai Water Vapor Cloud Impacts Its Transport Through the Stratosphere: Dynamical and Radiative Effects. *Geophysical Research Letters* **50** (2023).
37. M. Abdelkader, G. Stenchikov, A. Pozzer, H. Tost, J. Lelieveld, The effect of ash, water vapor, and heterogeneous chemistry on the evolution of a Pinatubo-size volcanic cloud. *Atmospheric Chemistry and Physics* **23**, 471-500 (2023).
38. S. A. Carn, L. Clarisse, A. J. Prata, Multi-decadal satellite measurements of global volcanic degassing. *Journal of Volcanology and Geothermal Research* **311**, 99-134 (2016).
39. G. Stenchikov, "Chapter 29 - The role of volcanic activity in climate and global changes" in Climate Change (Third Edition)*,* T. M. Letcher, Ed. (Elsevier, 2021), https://doi.org/10.1016/B978-0-12-821575-3.00029-3, pp. 607-643.
40. W. Read, L. Froidevaux, J. Waters, Microwave limb sounder measurement of stratospheric SO2 from the Mt. Pinatubo Volcano. *Geophysical Research Letters* **20**, 1299-1302 (1993).
41. A. Ukhov *et al.*, Inverse Modeling of the Initial Stage of the 1991 Pinatubo Volcanic Cloud Accounting for Radiative Feedback of Volcanic Ash. *Journal of Geophysical Research: Atmospheres* **128** (2023).
42. M. McCormick, R. Veiga, SAGE II measurements of early Pinatubo aerosols. *Geophysical Research Letters* **19**, 155-158 (1992).
43. B. Legras *et al.*, The evolution and dynamics of the Hunga Tonga–Hunga Ha'apai sulfate aerosol plume in the stratosphere. *Atmospheric Chemistry and Physics* **22**, 14957-14970 (2022).
44. M. L. Santee *et al.*, Strong Evidence of Heterogeneous Processing on Stratospheric Sulfate Aerosol in the Extrapolar Southern Hemisphere Following the 2022 Hunga Tonga‐Hunga Ha'apai Eruption. *Journal of Geophysical Research: Atmospheres* **128** (2023).

45. P. B. Russell *et al.*, Global to microscale evolution of the Pinatubo volcanic aerosol derived from diverse measurements and analyses. *Journal of Geophysical Research: Atmospheres* **101**, 18745-18763 (1996).
46. J. J. Bauman, P. B. Russell, M. A. Geller, P. Hamill, A stratospheric aerosol climatology from SAGE II and CLAES measurements: 2. Results and comparisons, 1984-1999. *Journal of Geophysical Research: Atmospheres* **108**, n/a-n/a (2003).
47. M. Sato, J. E. Hansen, M. P. McCormick, J. B. Pollack, Stratospheric aerosol optical depths, 1850–1990. *Journal of Geophysical Research: Atmospheres* **98**, 22987-22994 (1993).
48. J. P. Vernier *et al.*, Major influence of tropical volcanic eruptions on the stratospheric aerosol layer during the last decade. *Geophysical Research Letters* **38** (2011).
49. A. Baron *et al.*, Early Evolution of the Stratospheric Aerosol Plume Following the 2022 Hunga Tonga‐Hunga Ha'apai Eruption: Lidar Observations From Reunion (21° S, 55° E). *Geophysical Research Letters* **50** (2023).
50. C. Duchamp *et al.*, Observation of the Aerosol Plume From the 2022 Hunga Tonga—Hunga Ha'apai Eruption With SAGE III/ISS. *Geophysical Research Letters* **50** (2023).
51. C. Kloss *et al.*, Aerosol Characterization of the Stratospheric Plume From the Volcanic Eruption at Hunga Tonga 15 January 2022. *Geophysical Research Letters* **49** (2022).
52. H. Vehkamäki *et al.*, An improved parameterization for sulfuric acid–water nucleation rates for tropospheric and stratospheric conditions. *Journal of Geophysical Research: Atmospheres* **107** (2002).
53. J. Zhao, R. P. Turco, O. B. Toon, A model simulation of Pinatubo volcanic aerosols in the stratosphere. *Journal of Geophysical Research: Atmospheres* **100**, 7315-7328 (1995).
54. P. A. Case *et al.*, Simulating Sulfate Aerosol Size in the Hunga Tonga Plume: Comparisons with Observations. *AGU23* (2023).
55. J. M. Rodriguez, M. K. Ko, N. D. Sze, Role of heterogeneous conversion of N2O5 on sulphate aerosols in global ozone losses. *Nature* **352**, 134-137 (1991).
56. D. R. Hanson, A. Ravishankara, S. Solomon, Heterogeneous reactions in sulfuric acid aerosols: A framework for model calculations. *Journal of Geophysical Research: Atmospheres* **99**, 3615-3629 (1994).
57. M. Prather, Catastrophic loss of stratospheric ozone in dense volcanic clouds. *Journal of Geophysical Research: Atmospheres* **97**, 10187-10191 (1992).
58. S. Evan *et al.*, Rapid ozone depletion after humidification of the stratosphere by the Hunga Tonga Eruption. *Science* **382**, eadg2551 (2023).
59. Y. Zhu *et al.*, Stratospheric ozone depletion inside the volcanic plume shortly after the 2022 Hunga Tonga eruption. *Atmospheric Chemistry and Physics* **23**, 13355-13367 (2023).
60. E. L. Fleming, P. A. Newman, Q. Liang, L. D. Oman, Stratospheric Temperature and Ozone Impacts of the Hunga Tonga‐Hunga Ha'apai Water Vapor Injection. *Journal of Geophysical Research: Atmospheres* **129** (2024).

61. K. Labitzke, M. McCormick, Stratospheric temperature increases due to Pinatubo aerosols. *Geophysical Research Letters* **19**, 207-210 (1992).
62. S. Chandra, Changes in stratospheric ozone and temperature due to the eruptions of Mt. Pinatubo. *Geophysical research letters* **20**, 33-36 (1993).
63. K. Labitzke, Stratospheric temperature changes after the Pinatubo eruption. *Journal of Atmospheric and Terrestrial Physics* **56**, 1027-1034 (1994).
64. M. R. Schoeberl *et al.*, The Estimated Climate Impact of the Hunga Tonga - Hunga Ha'apai Eruption Plume. *Geophysical Research Letters* **50** (2023).
65. J. W. Waters *et al.*, The Earth observing system microwave limb sounder (EOS MLS) on the aura Satellite. *IEEE Transactions on Geoscience and Remote Sensing* **44**, 1075-1092 (2006).
66. G. Taha *et al.*, OMPS LP Version 2.0 multi-wavelength aerosol extinction coefficient retrieval algorithm. *Atmos. Meas. Tech.* **14**, 1015-1036 (2021).
67. L. S. Szatkowski *et al.* (1999) Stratospheric aerosol and gas experiment III (SAGE III) mission aboard the International Space Station. in *Optical Spectroscopic Techniques and Instrumentation for Atmospheric and Space Research III* (SPIE), pp 164-171.
68. N. J. Livesey, W. V. Snyder (2004) EOS MLS retrieval processes algorithm theoretical basis. (Jet Propulsion Laboratory).
69. H. C. Pumphrey, W. G. Read, N. J. Livesey, K. Yang, Observations of volcanic SO2 from MLS on Aura. *Atmospheric Measurement Techniques* **8**, 195-209 (2015).
70. G. E. Nedoluha *et al.*, Increases in middle atmospheric water vapor as observed by the Halogen Occultation Experiment and the ground-based Water Vapor Millimeter-Wave Spectrometer from 1991 to 1997. *Journal of Geophysical Research: Atmospheres* **103**, 3531-3543 (1998).
71. H. M. Steele, P. Hamill, Effects of temperature and humidity on the growth and optical properties of sulphuric acid—water droplets in the stratosphere. *Journal of Aerosol Science* **12**, 517-528 (1981).
72. I. N. Tang, H. R. Munkelwitz, Water activities, densities, and refractive indices of aqueous sulfates and sodium nitrate droplets of atmospheric importance. *Journal of Geophysical Research* **99** (1994).
73. I. N. Tang, Chemical and size effects of hygroscopic aerosols on light scattering coefficients. *Journal of Geophysical Research: Atmospheres* **101**, 19245-19250 (1996).
74. J. Wang, S. T. Martin, Satellite characterization of urban aerosols: Importance of including hygroscopicity and mixing state in the retrieval algorithms. *Journal of Geophysical Research* **112** (2007).
75. J. H. Seinfeld, S. N. Pandis (2016) Atmospheric chemistry and physics : from air pollution to climate change. (John Wiley & Sons, Hoboken, New Jersey).
76. D. Fussen, F. Vanhellemont, C. Bingen, Evidence of transport, sedimentation and coagulation mechanisms in the relaxation of post-volcanic stratospheric aerosols. *Ann. Geophys.* **19**, 1157-1162 (2001).

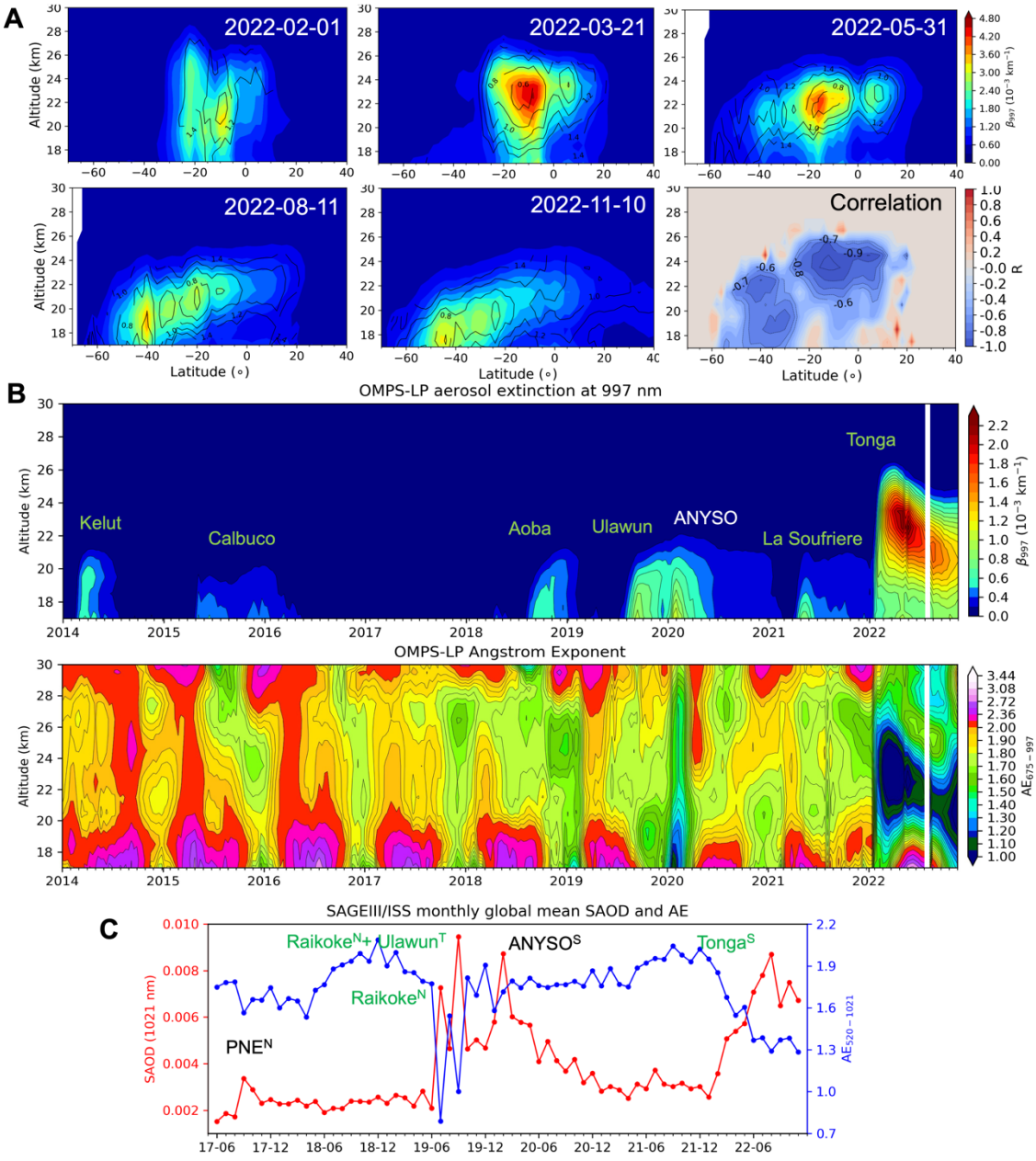
77. M. Kulmala, A. Laaksonen, L. Pirjola, Parameterizations for sulfuric acid/water nucleation rates. *Journal of Geophysical Research: Atmospheres* **103**, 8301-8307 (1998).
78. M. P. Baldwin *et al.*, The quasi‐biennial oscillation. *Reviews of Geophysics* **39**, 179-229 (2001).
79. M. R. Schoeberl *et al.*, QBO and annual cycle variations in tropical lower stratosphere trace gases from HALOE and Aura MLS observations. *Journal of Geophysical Research: Atmospheres* **113** (2008).
80. P. Ricaud *et al.*, Equatorial transport as diagnosed from nitrous oxide variability. *Atmos. Chem. Phys.* **9**, 8173-8188 (2009).
81. M. Park *et al.*, Variability of Stratospheric Reactive Nitrogen and Ozone Related to the QBO. *Journal of Geophysical Research: Atmospheres* **122** (2017).
82. K. F. Palmer, D. Williams, Optical Constants of Sulfuric Acid; Application to the Clouds of Venus? *Applied Optics* **14**, 208-219 (1975).
83. G. L. Stenchikov *et al.*, Radiative forcing from the 1991 Mount Pinatubo volcanic eruption. *Journal of Geophysical Research: Atmospheres* **103**, 13837-13857 (1998).

Figures and Tables



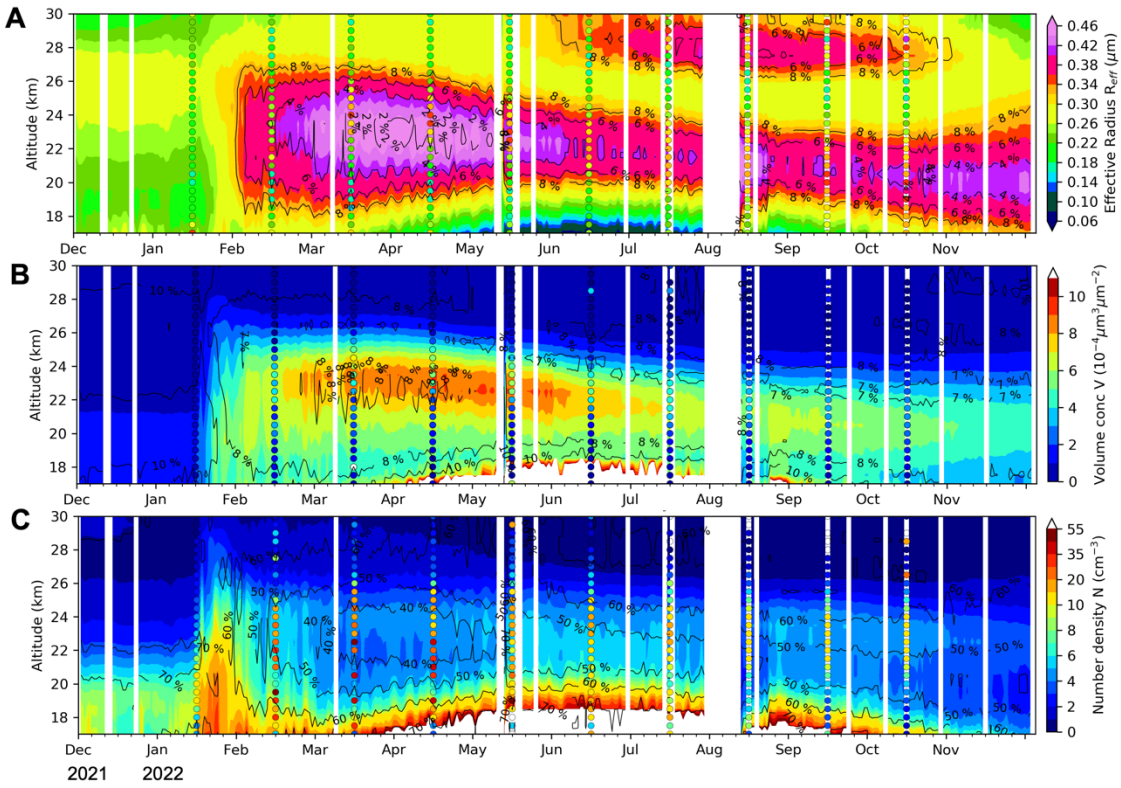
880 **Figure 1. The transport and evolution of stratospheric WV observed from space after HT.** (**A**) The spatial distribution of OMPS-NM STL SO_2 column density for 20-23 December 2021 and 14-15 January 2022. The maximum SO_2 column density among all pixels in the region of each

panel is denoted following “Max”. The location of the HT volcano is denoted as a magenta triangle in each panel. The red arrows indicate the diffusion directions of SO_2 plume based on the plume shape and location. (**B**) The daily averaged zonal distribution of MLS v4.2 (without quality control, no QC) WV VMR profiles between 70˚S to 70˚N on different days, as noted in each panel. (**C**) The stratospheric SO_2 (red) and WV mass anomaly in 0˚-30˚S estimated from MLS v5.0 (green) and v4.2 (blue) data with (dashed) or without (solid) QC. Gray solid line shows the WV mass anomaly in 70˚S-70˚N from MLS v4.2 without QC. Note that the decreasing of WV anomaly mainly comes from zonal transport to other latitudes instead of removal from the stratosphere.



895 **Figure 2. The evolution of vertical profiles of aerosol extinction and Angstrom exponent (AE) after HT and their correlation.** (**A**) OMPS-LP daily zonal distribution of the aerosol extinction coefficient at 997 nm (β_{997}, background pattern) and AE between 675 and 997 nm ($AE_{675\text{-}997}$, contour lines, shown only for β_{997}> 0.0003 km^{-1}) profiles on different days, as noted in each panel. The lower right panel shows the zonal distribution of the correlation coefficient *R* 900 between β_{997} and $AE_{675\text{-}997}$ daily profiles from HT to the end of November 2022 (only for β_{997} > 0.0005 km^{-1}). (**B**) OMPS-LP 10-day mean β_{997} (top) and $AE_{675\text{-}997}$ (bottom) from January 2014 to November 2022 averaged over 20˚N-30˚S. (**C**) SAGE III/ISS global monthly average SAOD at 1021 nm (red) and $AE_{520\text{-}1021}$ (blue) in 2017-2022. The names of big volcanic eruptions (green) and wildfire injections (black) are noted (PNE: Pacific Northwest Event; ANYSO: Australian New

905 Year Super Outbreak), and the superscript indicates the event locations (N: Northern hemisphere; T: Tropics; S: Southern hemisphere).



910 **Figure 3. The evolution of R_{eff} (A), V (B), N (C) in 0˚-30˚S retrieved from satellite observed AE and β_{997} for HT sulfate particles after 1 December 2021.** OMPS-LP daily mean profiles are shown as background and overlapped by SAGE III/ISS monthly mean profiles shown on the 15th of each month (circles). The relative uncertainties (percentages) of each parameter retrieval from OMPS-LP due to different σ in the particle size distribution (see details in Materials and Methods)
915 are highlighted by the black contour lines in each panel.

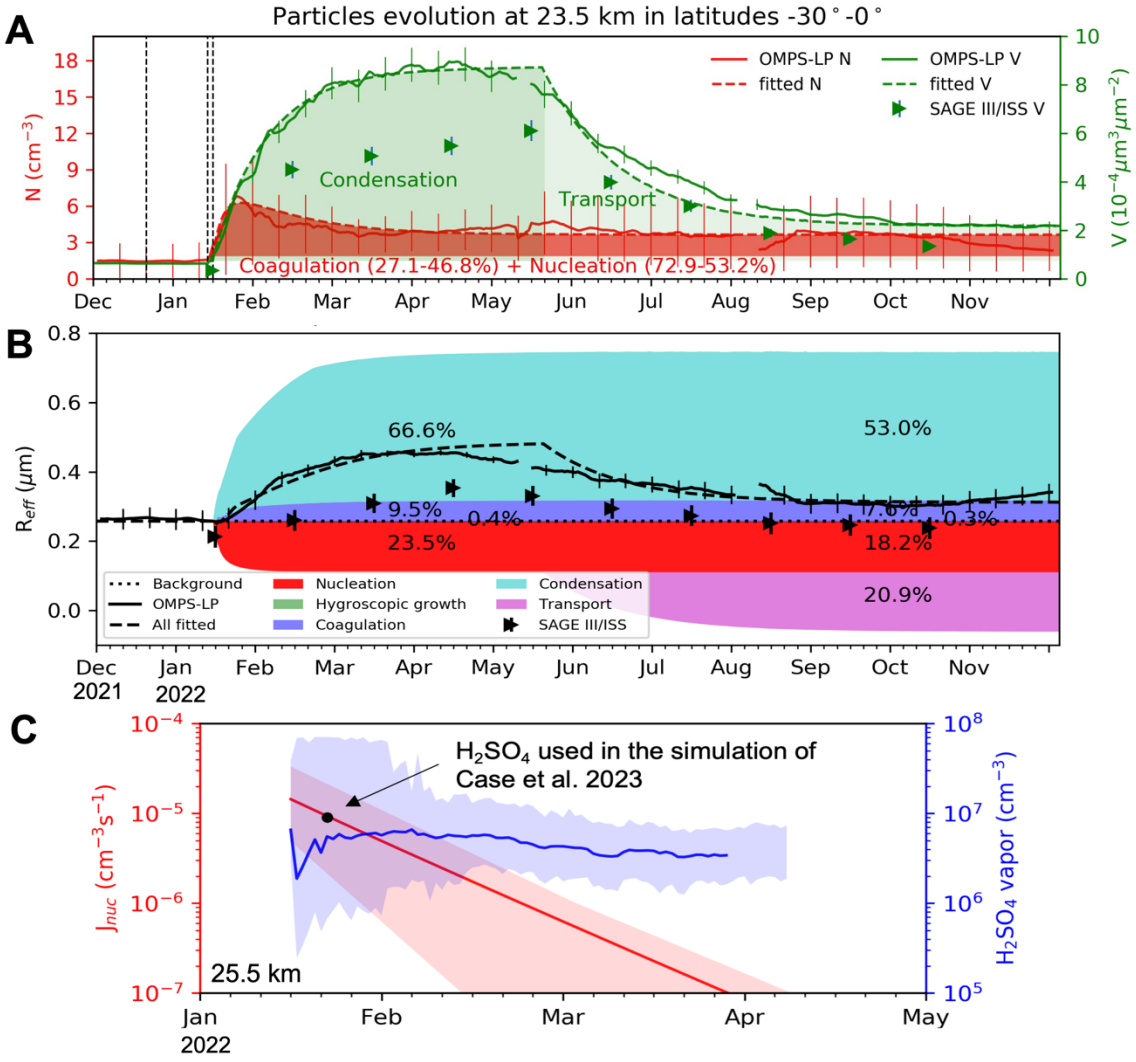


Figure 4. Comparison of OMPS-LP daily (solid lines with error bars representing the uncertainties due to different σ values in the particle size distribution) and SAGE III/ISS monthly (triangles with similar error bars) *V* (green in A), *N* (red in A) and R_{eff} (black in B) at 23.5 km averaged in 0˚-30˚S with ODEs fitted results (dashed lines). (A) Black vertical dashed lines show the HT eruption dates. The shaded areas represent the *V* and *N* anomalies caused by single (green) or multiple microphysical processes (red) as noted. The dark green and light green shades reveal the periods when condensation or transport dominated. The percentages following process names indicate the contribution of each process on *N* anomaly averaged in the first 10 days (left) and subsequent days (right). **(B)** The filled areas indicate the possible evolution of R_{eff} when only single process happens. The relative percentage contribution of each process on R_{eff} anomaly on 20 March (left) and 16 September (right), 2022 are highlighted on the figure. The black dotted line shows the background R_{eff} value. **(C)** The timeseries of nucleation rates (J_{nuc}, red) and H_2SO_4 vapor concentration (blue) derived from ODE fitting results at 25.5 km in 0˚-30˚S. The red shadow indicates the range of J_{nuc} caused by different σ assumptions used in PSD, while the blue shadow represents the uncertainties due to both different σ and RH values in 0˚-30˚S. Correspondingly, the red and blue solid lines represent

the median values of J_{nuc} and H_2SO_4 vapor concentration, respectively. The black dot indicates the H_2SO_4 vapor concentration used in the simulation from a microphysical box model in Case*, et al.* (54) (see details in the supplementary Text S6).

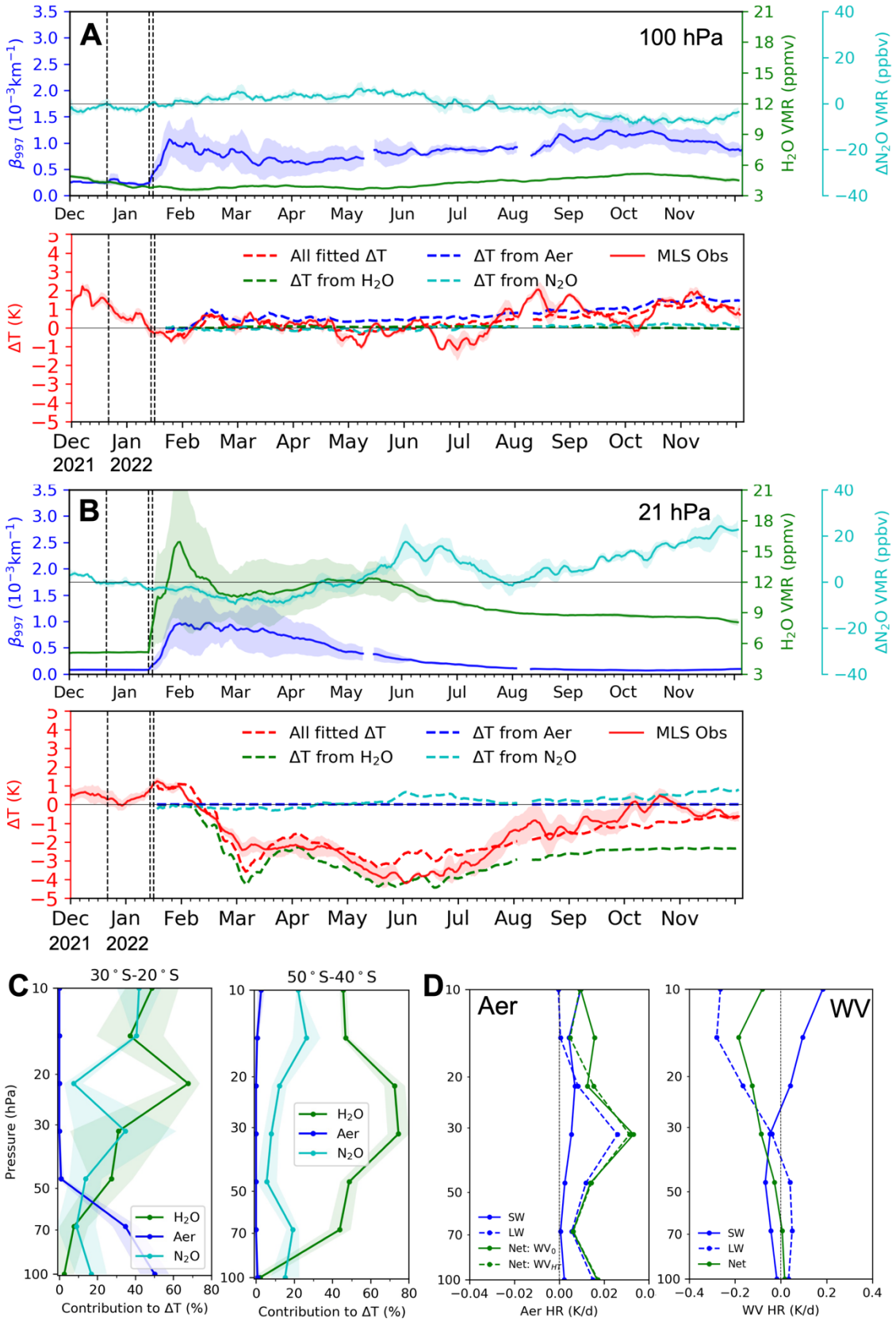

A
100 hPa
B
21 hPa
β_{997} (10^{-3}km^{-1})
H$_2$O VMR (ppmv)
ΔN$_2$O VMR (ppbv)
ΔT (K)
All fitted ΔT
ΔT from Aer
MLS Obs
ΔT from H$_2$O
ΔT from N$_2$O
Dec Jan Feb Mar Apr May Jun Jul Aug Sep Oct Nov
2021 2022
C
30°S-20°S
50°S-40°S
Pressure (hPa)
H$_2$O
Aer
N$_2$O
Contribution to ΔT (%)
D
Aer
WV
SW
LW
Net: WV$_0$
Net: WV$_{HT}$
Net
Aer HR (K/d)
WV HR (K/d)

Figure 5. The evolution of MLS temperature anomaly compared with OMPS-LP aerosol extinction ($\boldsymbol{\beta_{997}}$), MLS WV, and N_2O anomalies. (**A**) Top: daily mean MLS WV VMR (green), N_2O VMR (cyan), and OMPS-LP $\boldsymbol{\beta_{997}}$ (blue) since 1 December 2021 in the subtropics (20˚S-30˚S) at 100 hPa (16-17 km). Bottom: MLS observed (solid line) and multi-variable linear regression fitted temperature anomalies (ΔT) of each factor ($\boldsymbol{\beta_{997}}$, WV and N_2O, dashed lines) in the same region and altitude as the top panel. The shadows indicate mean ± standard deviation ranges in the region. Black vertical dashed lines show the HT dates. (**B**) The same as (**A**) but for 21 hPa (~26 km). (**C**) The percentage of contribution from each factor to absolute temperature anomaly at 10-100 hPa averaged in the subtropics and mid-latitudes (40˚S-50˚S) (see Methods). (**D**) The SW, LW and net heating rate profiles in 20˚S-30˚S from enhanced aerosols (left) and WV (right) after HT eruption. WV_0 represents the calculation using background WV concentration before HT eruption while WV_{HT} is the result using enhanced WV after HT eruption in Fu-Liou model.